3D Flow Modelling of the Medium-Term Circulation Test Performed in the Deep Geothermal Site of Soultz-Sous-forêts (France)

Sylvie Gentier, Xavier Rachez, Tien Dung Tran Ngoc, Mariane Peter-Borie, Christine Souque

3D Flow Modelling of the Medium-Term Circulation Test Performed in the Deep Geothermal Site of Soultz-Sous-forêts (France)

Sylvie Gentier, Xavier Rachez, Tien Dung Tran Ngoc, Mariane Peter-Borie, Christine Souque

BRGM, Geothermal Department, 3 Av. Claude Guillemin, BP 36009, Orléans - France

s.gentier@brgm.fr

Keywords: DFN, flow, fractures, Soultz-sous-Forêts, transport model

ABSTRACT

Three boreholes have been drilled at 5-km depth within the fractured granite of the Soultz-sous-Forêts geothermal site (France). A five-month circulation test, joint with a tracer test, have been performed in 2005 between the injection well GPK3 and the production wells GPK2 and GPK4. After an analysis by a method of dispersive transfer model of the experimental breakthrough curves (BTC), three main circulation loops within the heat exchanger have been obtained.

The aim of our work is to build a flow model of the Soultz-sous-Forêts fractured reservoir, based on a realistic fracture network from a hydraulic point of view and consistent with the knowledge of the regional tectonic history. In this paper, the first stages of this model are presented.

The proposed conceptual fracture model is based on five main fracture sets that constitute the reservoir in itself, and on some deterministic fault zones that condition the access from the well to the statistical fracture network to the three open holes.

On the basis of fracture data collected from well imagery, new fracture density distributions based on Fisher distribution have been calculated. Four main fracture sets corresponding to main statistical modes are individualised: two ~N-S striking sets respectively W-dipping and E-dipping; and two NE-SW and NW-SE striking sets respectively NW-dipping and SW-dipping. Those four main sets are consistent with the strain history. Indeed, two ~N-S striking sets respectively W-dipping and E-dipping are widely observed in the Rhine Graben and are commonly interpreted as the result of Oligocene deformation, but could also be related to lower Carboniferous to Permian NNE-SSW sinistral faulting. In addition, the two NE-SW and NW-SE striking sets are consistent with the orientation of the Hercynian structures observed regionally. A fifth fracture set is introduced in order to incorporate the "background noise".

Following this, a Discrete Fracture Network (DFN) model has been built. The rock matrix is considered as impermeable, and the fluid flow takes place only within the fractures. Tracer transport is solved by the particle tracking method.

At this stage of progress, the fracture model tends to reproduce the GPK2 breakthrough curve obtained during the medium-term circulation test performed between the three wells. The GPK2 breakthrough peak is mainly due to the two ~N-S striking sets which constitute the shortest paths between GPK3 and GPK2 while its tail is rather due to the two other main fracture sets, NE-SW and NW-SE

striking which create longer paths between GPK3 and GPK2 than the two ~N-S striking sets. However, it seems impossible to define a unique homogeneous statistical fracture model leading to a simultaneous fit of the two wells GPK2 and GPK4. The work in progress lets assume that a regional evolution of the basic pattern could be a solution. At this stage, it appears that the NE-SW and NW-SE striking sets could play a role more important between GPK3 and GPK4 than between GPK3 and GPK2.

1. INTRODUCTION

The experiments initiated at the Soultz-sous-Forêts site (France) in 1987 aim at producing electricity from the heat available in the granite basement. To do so, three boreholes have been drilled down to 5 km depth. Heat is extracted with this geothermal boreholes triplet by injecting fresh fluid in one of the three wells (the injection well, GPK3) and by pumping hot fluid from the two other wells (the production wells, GPK2 and GPK4).

A five-month circulation test, coupled with a tracer test, was performed in 2005 between the three wells. It represented the first real circulation test between the triplet at 5-km depth within which the circulation will take place in the future exploitation scheme. The circulation test involved a closed loop between the injection well GPK3 (15×10^{-3} m³/s) and the two production wells GPK2 (-12×10^{-3} m³/s) and GPK4 (-3×10^{-3} m³/s). No production pump was deployed inside the production wells for the experiment. All the produced water was re-injected. A tracer test using 150 kg of 82.5% pure fluorescein was performed during the five-month circulation experiment. At the end of the test, the total fluorescein recovery through GPK2 has been estimated as 23.5%. The total fluorescein recovery through GPK4 has been estimated as 1.8% of the fluid injected into GPK3. The results obtain from GPK2 are consistent with those obtained in 1997 between GPK1 and GPK2 at shallower depth (Aquilina *et al.*, 1998). A strong dissimilarity in the shape of the breakthrough curves of GPK2 and GPK4 has to be noticed (Figure 1).
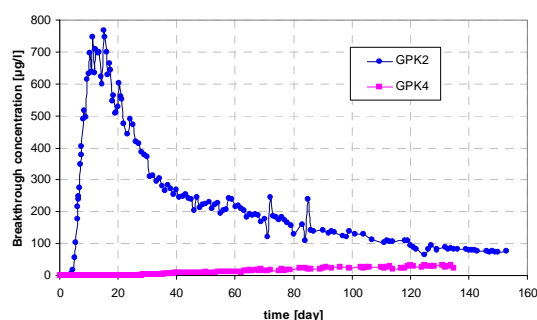

Figure 1: Fluorescein concentration in the fluid discharged from GPK2 and GPK4.
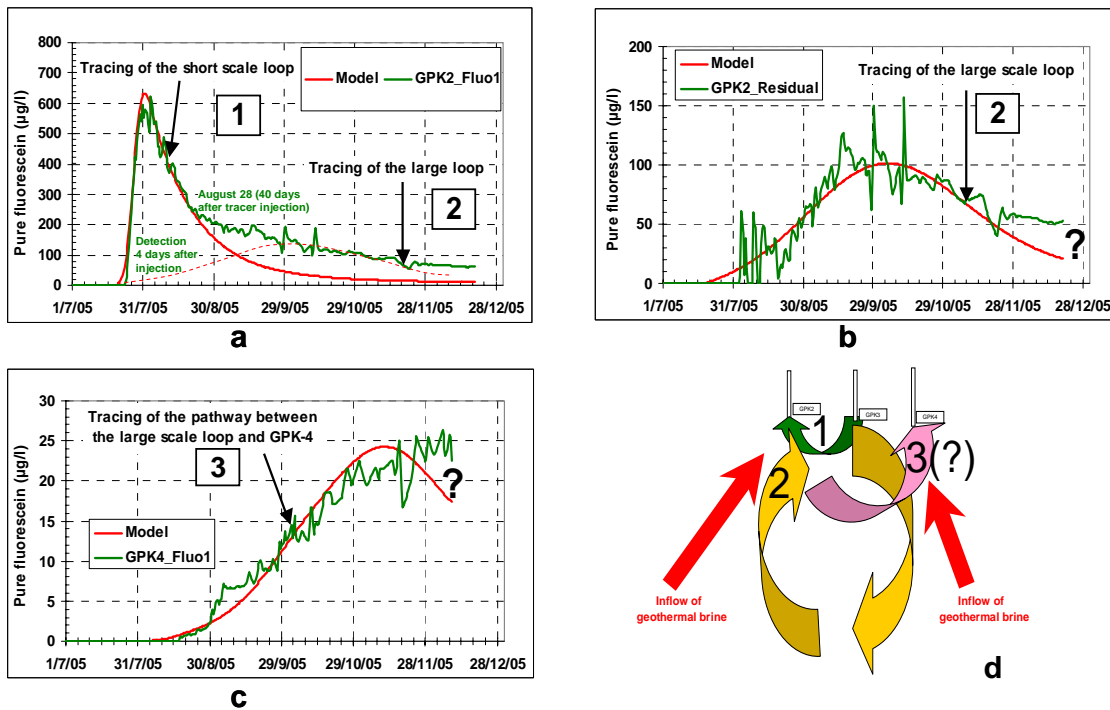
Figure 2: Fitting of the fluorescein recovery in the fluid discharged from GPK-2 (a and b) and GPK4 (c) using a dispersive transfer model and conceptual model of fluid circulation in the Soultz geothermal exchanger (d) (Sanjuan *et al.* 2006, modified).

A first analysis by signal processing of the tracer restitution curves (Sanjuan *et al.*, 2006) gave evidence of a fast and relatively direct hydraulic connection between the wells GPK3 and GPK2 - short loop - but also indicated the existence of another larger and slower hydraulic connection between the wells - large loop - (Figure 2).

Blumenthal *et al.* (2007) proposed a simulation of the hydraulic and thermal processes involved in the heat reservoir of Soultz-sous-Forêts. Their 2D model is supposed to be as simple as possible (Figure 8a) taking into account the major structural units only with as few parameters as possible to reduce the degree of freedom (permeability, porosity). Structural elements included in the model consist in 1) two dominant natural fracture sets, 2) hydraulically stimulated around the wells, 3) with major fracture zone 4) connecting the three wells. From a reference simulation (Figure 8b) used to perform a parameter study, the best adjustment to the measured data presented by the authors is illustrated on Figure 8c. Although breakthrough time and maximum tracer concentration match very well, tailing and final concentration do not agree with the measured data. After the authors, the discrepancies might be due to neglected 3D effects. Nevertheless, the adjusted simulation fits the data in three aspects: (1) The time of tracer breakthrough; (2) The maximum tracer concentration; (3) The amount of tracer recovery.

Considering the small amount of available data and the lack of comprehensive geological reference mode, a 3D model restricted to the geothermal reservoir between GPK2 and GPK3 based on inverse methods (deterministic Bayesian methodology) has been proposed by Gessner *et al.* (2009). The 3D geometry Gessner *et al.* (2009) proposed is close to the 2D geometry of Blumenthal *et al.* (2007) considering four units (1: background rock, 2 and 3: major fracture

connecting the wells and 4: stimulated zones around the wells). Results about the combination between porosity and permeability led the authors to interpret them as characteristic for fractured media with very few fractures of comparatively large width. To limit the computing time, authors limited the number of parameters inverted (porosity, isotropic permeability and in some cases dispersivity). For future models, the authors advise to use more independent data such as pressure and temperature observations from hydraulic well tests.

To go further in the understanding of the flow paths between the wells, a 3D transport model by a Discrete Fracture Network (DFN) approach is under progress based on the geological and structural knowledge of the deep granite massif. The comprehensive approach and first results are presented hereafter.

2. GEOLOGICAL FRACTURE MODEL

A basic step of the DFN modeling is to define a 3D fracture network model from the *in situ* observations made, in our case, in boreholes. The proposed fracture model is based on two types of fractures:

- A network of fracture sets in the granite massif. Fracture data obtained from borehole imagery techniques in non rectilinear wells (about 5 000 fractures identified by Dezayes *et al.,* 2005) constitute an incomparable database. This database is analysed with specific statistical and probabilistic methods to define the main fracture sets, and to estimate their spatial distribution;

- Fault zones well-identified in each well by fluid loss (Sausse *et al.*, 2007) and that are consequently assumed to play a role in the connection between the well and the reservoir. It should be noticed that, as no

log is available in GPK2 between 3 800 m and 5 100 m (length along borehole), direction and dip of the fault zones in this well have been estimated from average major directions of fracture in the Soultz granite : N160°E-65/70°NE and SW (Dezayes *et al.*, 2008 ; Sausse *et al.*, 2008). Moreover, although no data on the fault zone extension are directly available, the well-known presence of kilometric faults in the Soultz Graben lets assume that the identified fault zones might have at least hectometric extensions (Dezayes *et al.*, 2008; Sausse *et al.*, 2008). A stereographic representation of the main fault zones is shown on Figure 3.
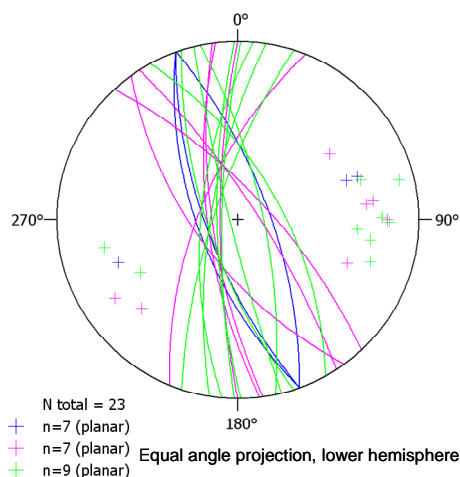

Figure 3: Stereographic representation of the major fault zones (in blue: GPK2, in pink: GPK3, in green: GPK4) issued from Sausse *et al.*, 2007.

2.1. Statistical Analysis of the Fracture Network

On the basis of the fracture data collected in wells GPK1, GPK2, GPK3 and GPK4 (Dezayes *et al.*, 2005), new fracture densities based on Fisher distribution have been computed. This method, useful to study large databases, allows to bring out sets of fractures that are represented by few entities and that could be masked by numerous fractures of major sets.

As shown Figure 4, four main fracture sets corresponding to main statistical modes are individualised. Their characteristics are given Table 1. Are recognised:

- Two ~N-S striking sets respectively W-dipping (F1) and ENE-dipping (F2);

- Two NE-SW and NW-SE striking sets respectively NW-dipping (F3) and SW-dipping (F4).

Moreover, the numerous fracture left outside the four main sets are gathered together in a fifth set (F5, N0 to 180°E-70°) corresponding to the "background noise".
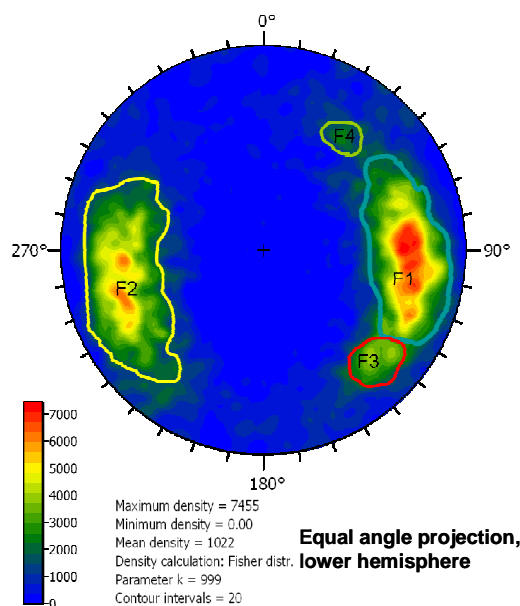

Figure 4: Stereographic representation of Fisher density distribution of fractures collected in wells GPK1, GPK2, GPK3 and GPK4 and identified sets of fractures.

2.2 Spatial Characteristics of the Fracture Sets

To define a 3D network of fractures from 1D data, it is necessary firstly to correct apparent fracture density from the well orientation, and secondly to estimate fracture length. By using a probabilistic approach, we propose to estimate the 3D density depending on the fracture length.

To estimate the probability of intersection of each fracture plane with each well, planes are randomly generated in a parallelepiped volume of 15 km^3 (dimension: E-W = 2 km ; N-S : 3 km ; vertical: 2.5 km – equal to the volume taken into account in the numerical model, see § 3.5). The number of planes of each set intersecting each well or fraction of well (GPK2, GPK3 and GPK4) is then counted. This procedure is repeated six times with different random draws. Two approaches have been considered. The first approach is to consider any fracture orientation in order to study the fracture network potentially hydraulically connected to each well in the open holes. A stereographic view of the result for all plane orientations is given Figure 5.

Table 1: Main statistical data of fracture sets

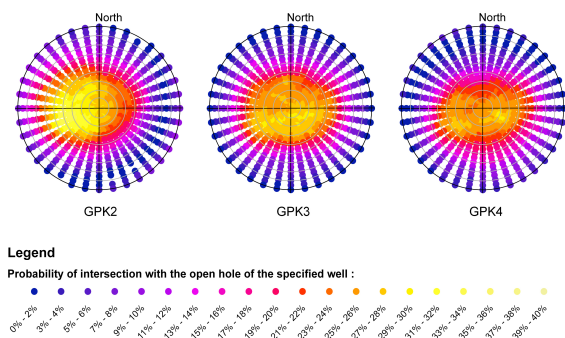| Set of fractures		F1	F2	F3	F4	F5
Direction and dip of the mean plane		N002-70°W	N162-70°ENE	N042-74°NW	N129-68°SW	N0 to N360 - 70°
Std deviation of the plane direction		16°	19°	6°	6°	
Standard deviation of the plane dip		7°	7°	3°	3°	9°
Distribution type (direction and dip)		normal	normal	normal	Normal	uniform (dip dir) normal (dip)
Eigen vector	cartesian coordinates	0.03, -0.94, -0.33	0.29, 0.89, -0.34	0.65, -0.71, -0.26	0.72, 0.59, 0.37	
	direction and dip	N272°E-19°NW	N252°E-19°	N132°E-15°	N39°E-21°	
Normalised length of the mean vector perpendic. to the mean plane		0.957	0.944	0.994	0.994	

Figure 5: Stereographic view (lower hemisphere) of the probability of intersection of planes (represented by their pole) with the open holes of the three wells.

Table 2: Probability of intersection of sets of planes with the wells from -3 500 m to the bottom of each well.

Probability [%] of intersection	of	fracture set with directions :			
		N 0 (~F1)	N 160 (~F2)	N40 (~F3)	N130 (~F4)
	with GPK2	8 $^{+/-1}$	33 $^{+/-2}$	3 $^{+/-1}$	20 $^{+/-2}$
	with GPK3	24 $^{+/-2}$	24 $^{+/-2}$	22 $^{+/-3}$	16 $^{+/-1}$
	with GPK4	31 $^{+/-2}$	23 $^{+/-2}$	37 $^{+/-2}$	10 $^{+/-1}$

Table 3: Estimation of fracture densities for infinite planes from observations and from probabilities.

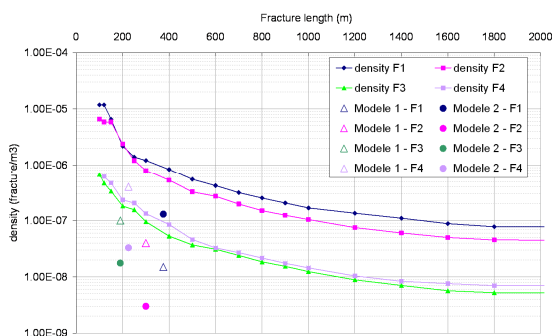|	Fracture set directions :			
Density	N0 (F1)	N160 (F2)	N040 (F3)	N130 (F4)
constructed from GPK3	6.5 10^{-8}	3.9 10^{-8}	7.2 10^{-9}	1.1 10^{-8}
constructed from GPK4	5.1 10^{-8}	3.7 10^{-8}	2.1 10^{-9}	3.4 10^{-9}
Mean	5.8 10^{-8}	3.8 10^{-8}	4.7 10^{-9}	7.2 10^{-9}

Figure 6: Densities for each fracture set introduced in the models in comparison with theoretical estimation.

The second approach is to consider only the mean orientation of the four main fracture sets to estimate densities and fracture lengths from -3 500 m to the bottom of each well, corresponding to the available data considered for our hydraulic model. The probability of intersection with each well is sum up in Table 2. The fracture densities are then estimated from the probability of intersection of each set of fractures with the trajectory of each well and the number of observed fractures in GPK3 and GPK4 (no observation is available for GPK2). Results are given Table 3 in a scenario of infinite planes. As no information on fracture length can be deduced by measured data from 1D line (intersections between the fracture network and the wells), this point is not well constrained. But, as the densities are fixed in each well, a volumetric density can be estimated as a function of fracture length. Figure 6 represents the relation between fracture lengths and densities for one random draw.

2.3. Discussion About Fracture Model

The statistical analyses allow to highlight four main fracture sets in the granite of Soultz-sous-Forêts. We can note that the selected major faults have orientations similar to those of the statistical sets, but all the statistical fracture sets do not correspond to major fault zones (Figure 3). Most of the selected faults belong to the two ~N-S striking sets (F1 and F2), some of them belong to NW-SE striking set (F4) and no belong to NE-SW striking (F3).

We propose here to discuss firstly, the consistency of the fracture network model with the tectonic and, secondly, the impact of the well trajectory on the likelihood of direct fracture connection to the wells.

2.3.1. Consistency with Tectonic and Geological Model

The present time fracture population observed in the granite from Soultz-sous-Forêts is the result of a succession of deformation through time. The granite intrusions got emplaced in the Visean time, the emplacement of the plutonic bodies being controlled by a NE-SW oriented sinistral shear (Schulmann *et al.*, 1997, Edel *et al.*, 2007). The granite then got fractured during the Hercynian orogeny and the Oligocene to actual Rhine Graben emplacement.

A large part of the fracturing observed in the granite is to be related to the Hercynian orogeny and particularly to the Carboniferous and Permian phases of wrench tectonics (Ziegler, 1990). From lower Carboniferous to Permian, NNE-SSW sinistral fault zones are developed, associated with dyke swarms (Schumacher, 2002). Few late Hercynian NW-striking dextral faults are also observed could be Riedel or conjugate faults to the previous. Illiès (1972), Schumacher (2002) and Edel *et al.* (2007), among others, underline the role of the reactivation of the Hercynian structures during the subsequent tectonic phases.

In the Mesozoic times, structures related to an E-W extension have been locally recognised by Bergerat (1985) and Villemin (1986). Then, the same authors identify during the Cenozoic four successive stages of deformation corresponding to the Rhine Graben emplacement:

(i) From middle to late Eocene, a N-S compression, related to the collisional phases in the Alps and Pyrenees, reactivates crustal Hercynian faults (Schumacher, 2002). Within the sedimentary cover, NNW and NNE striking conjugate strike-slip faults are generated;

(ii) From late Eocene to late Oligocene, a E-W extension generated N-S structures in the sedimentary cover of the graben curbs and a period of subsidence in the graben (maximum subsidence in the southern part of the graben);

(iii) From late Oligocene to early Miocene, a NE-SW compression reactivates the graben as a dextral strike-slip

system (Schumacher, 2002) and N-S to NNE-SSW and NE-SW to E-W strike-slip faults are recognised;

(iv) Finally, from late Miocene and up to present, a NW-SE compression reactivates the graben as a sinistral strike-slip system (Schumacher, 2002) and N-S to NNW-SSW and E-W strike-slip faults are recognised.

The Palaeozoic deformation is likely to impact the Oligocene strain localisation and the extent of fracturing associated with the Oligocene to present deformation. In particular, some fault zones NW-SE striking and steeply dipping to the SW, consistent with one of the Hercynian orientation associated with dyke intrusions, are recognised on the UBI images. It can be observed that these faults play a leading role in the injection tests and the microseismic activity recorded during the hydraulic stimulation (Cuenot *et al.*, 2008). Cuenot *et al.* (2008) show that they are not through-going regional features but are of limited extent.
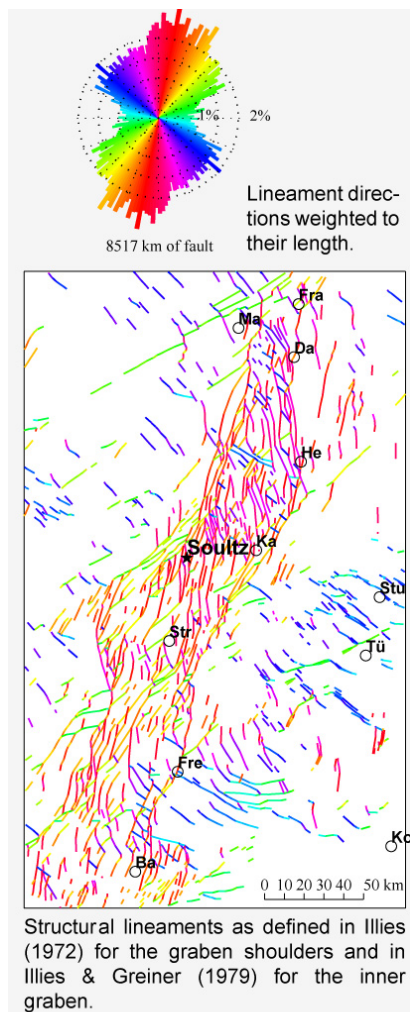

Figure 7: Structural lineament observed in surface and their orientation distribution. After Valley (2007).

The statistical treatment of the fracture data obtained from borehole images (UBI) in order to build a statistical model individualised four main sets of fracture:

- The two ~N-S striking sets respectively W dipping (F1) and E dipping (F2) are widely observed in the Rhine Graben (cf. red and pink structural lineaments on Figure 7) and are commonly interpreted as the result of Oligocene deformation, but could also be

related to lower Carboniferous to Permian NNE-SSW sinistral faulting;

- The two NE-SW and NW-SE striking sets (respectively F3 and F4) are consistent with the Hercynian structure orientations observed regionally (cf. blue and green structural lineaments on Figure 7).

The different sets of fracture observed at depths are thus consistent in orientation with the observations acquired regionally from fieldwork and aerial photography.

2.3.2. Impact of the Well Trajectories on the Fracture Observations

In such network of fractures, as shown by Figure 5 and Table 2, the probability of intersection of the non-rectilinear wells varies with each well and its depth.

The distribution of the probability of intersection of planes with the three open holes (Figure 5) presents globally an ellipsoidal shape with its major axis oriented E-W, favouring N-S striking sets (F1 and F2).

This elongation is particularly pronounced for GPK4. On Table 2, note that the GPK4 trajectory intersects with an equal probability the fracture sets with the direction N 0 (~F1) and N040 (~F3). GPK4 is less likely to intersect fractures with directions N160 (~F2) and still less N130 (~F4). These small variations between probability for the open hole (favourable for N-S striking fracture sets F1 and F2) and for the whole well from – 3 500 m (favourable for one N-S striking set F1 and a NE-SW striking set F2) are the consequences of not rectilinear trajectory. Probability of intersection varies with depth.

The ellipsoidal distribution is less significant for GPK3, which trajectory intersects with an equal probability the fracture sets striking N0 (~F1), N160 (~F2) and N040 (~F3); N130 (~F4) is a little bit less favourably oriented.

The probability of intersection of planes with the GPK2 open hole is particularly asymmetrically distributed. The planes which have the largest probability to cut the GPK2 open hole are mainly E-dipping. This observation is consistent with the fact that this well is preferentially cut by the fracture sets N162°-70°ENE (F2), and to a lower extent by N129°-68SW (F4, Table 2). The probability of intersection with a fracture set with directions N 0°-70W (~F1) and N042-74NW (~F3) is around 8% and 3%, respectively. This result could call into question the choice made for the deterministic fault zone directions retained for GPK2 (see § 2 and Figure 3).

The three open holes are most favourably oriented to allow direct transit through the fracture set N162 (F2): the orientation of this fracture set, coupled to the well trajectory, made this set potentially significant on a hydraulic point of view.

3. CONSTRUCTION OF THE NUMERICAL MODEL

3.1 Short Description of the Numerical Code Used

In the chosen DFN approach using code 3FLO (Itasca, 2006), the rock matrix is considered as impermeable, and the fluid flow takes place only within fractures. Only one fluid is considered. The impact of fluid density difference between the fresh water and the native brine on the hydraulic tests is therefore not taken into account. Neither the rock-fluid chemical interaction nor the thermal effect are here considered.

Table 4: Characteristics of the statistical fracture sets taken into account in the second model, and densities and hydraulic properties obtain after fitting.

| Fracture set # | Plane direction | | | Dip | | | | Number of fractures centers/m³ | Radius [m] | Transmissivity [m²/s] |
	Distribution law used	Mean	Half-width	Distribution law used	Mean	Half-width	Dip direction			
F1	Normal	2	16	Normal	70	7	NW	$1.30\ 10^{-7}$	187	$6.0\ 10^{-6}$
F2	Normal	162	19	Normal	70	7	NE	$3.00\ 10^{-9}$	150	$6.0\ 10^{-6}$
F3	Normal	42	6	Normal	74	3	NW	$1.76\ 10^{-8}$	95	$4.0\ 10^{-6}$
F4	Normal	129	6	Normal	68	3	SW	$3.30\ 10^{-8}$	112	$2.0\ 10^{-6}$
F5	Uniform	0	180	Normal	70	9	--	$1.00\ 10^{-8}$	100	$5.0\ 10^{-7}$

The fractures are simulated by disk-shape fracture planes. As each fracture plane is defined by its centre and the disk radius, the model requires to define, for each fracture set, a disk radius (considered as constant for a set) and a centre density per unit of volume. To generate flow paths through the fracture network, a network of channels (called pipes) is generated on each fracture. The connection of the channels from one plane to another through the fracture planes intersections (called tubes), constitutes *in fine* a 3D network of 1D elements.

The flow equation is solved in 1D classical Finite Elements:

$$C\ \frac{\partial^2 h}{\partial x^2} S_s = A_{Si}\ S_{Si}\ \frac{\partial h}{\partial t} \qquad (1)$$

where C [L³T⁻¹] is the pipe conductivity; h [L] is the hydraulic head; x [L] is the abscissa along of an element; A_{Si} [L²] is the element section; S_{Si} [L⁻¹] is the specific storage coefficient and t [T] is the time variable.

A pipe is formed by two infinite parallel ribbons, open enough so that a flow regime like the flow between two parallel plates can take place. In order to satisfy the laminar flow regime which dominates in rock masses (Louis, 1976), the pipe conductivity is correlated to the cubic law. The pipe section is then proportional to the cubic root of its conductivity. Therefore, the greater the pipe conductivity is, the greater the pipe volume is, and hence, the greater the porosity of the massif is. It is possible to define the pipe intrinsic storage coefficient S_{si} so that the global storage S_s of the reservoir satisfies the following relation:

$$S_s = \frac{\sum\limits_{pipe}(V_i * S_{si})}{\sum\limits_{pipe} V_i} \qquad (2)$$

where V_i [L³] is the pipe volume (pipe section A_{Si} × pipe length d [L]).

The two hydraulic parameters that are used to fit a flow model are therefore the pipe conductivity C [m³/s] and the storage coefficient S_s.

For a flow plane with a regularly spaced grid of channels, the fracture transmissivity T [m²/s] can be deduced from pipe conductivity C and the size d [L] of the grid with the following relation:

$$T_{[m²/s]} = \frac{C_{[m^3/s]}}{d_{[m]}} \qquad (3)$$

Solute transport is solved by using the Random Walk method. Flow is one-dimensional everywhere in pipes and tubes, except at their intersections. Dispersion is therefore only longitudinal, and is "completed" by the full mixing occurring at intersections. A pipe porosity n [-] can be specified, as well as a pipe dispersivity λ [L]. In a pipe, the particle displacement is rectilinear and uniform:

$$x = x + \frac{u.\Delta t}{n} \qquad (4)$$

where x [L], u [LT¹], Δt [T] and n are the particle position along the pipe, the fluid speed, the time step, and the pipe porosity, respectively.

3.2 Construction of the Numerical Fracture Models

The basic conceptual fracture model used to build the hydraulic model is based on the geological model presented in § 2 and contains 1) a network of statistical fractures, including the different fracture directions constituting the reservoir in itself; 2) deterministic fault zones identified in the wells and playing a role in the connection of the wells to the reservoir, and potentially activated during the hydraulic stimulation tests.

In a first time, large deterministic fault zones derived from Sausse *et al.* (2008) have been considered with a radius ranging from 500 m to 1 000 m. In this case, direct connections between wells are allowed. The statistical fracture network is issued from a first coarse statistic study. This network is formed by the four main fracture sets (F1 to F4, see § 2.1) with uniform distribution laws for dip and dip directions. Figure 9a represents a horizontal slice of this first 3D fracture model. This model is detailed in Gentier *et al.*, 2009 and not repeated in the present paper.

A second model has been built on the basis of:
- A more detailed analysis on the fractures data, described § 2.1. This led to generate five main fracture sets with normal distribution laws for the dip and dip direction, whose main statistical characteristics are exposed Table 4;

- Deterministic fault zones (see Table 5) with radii ranging from 50 m to 100 m. These deterministic fault zones do not correspond here to direct connection between wells but only condition the

access between from the wells to the statistical fracture network. To be more in accordance with the probability of intersection of fracture sets with the well GPK2 (see § 2.2 and discussion § 2.3.2) direction and dip have been modified. A reduced number of deterministic fault zones have been considered in GPK4, because of the lack of flow data in the deepest part of the well.

Table 5: Geometry of the deterministic fault zones cut by GPK2, GPK3 and GPK4 taken into account in the fracture model.

Name in Sausse al. (2007)	Plane Direction [°]	Dip [°]		Depth [m NGF]	Well where is generated the disk	Disk radius [m]	Transmissivity [m²/s]	Set of fractures
2-A'	171	69	SW	-4242	GPK2	50	5 10⁻⁷	F1
2-A"	172	67	NE	-4242	GPK2	50	5 10⁻⁷	F2
2-B	160	70	NE	-4305	GPK2	50	5 10⁻⁷	F2
2-C'	154	73	NE	-4372	GPK2	50	5 10⁻⁷	F2
2-D'	135	70	SW	-4564	GPK2	100	5 10⁻⁷	F4
2-E	160	65	SW	-4663	GPK2	50	5 10⁻⁷	F1
2-F'	137	71	NE	-4783	GPK2	100	5 10⁻⁷	F2
2-G	160	70	SW	-4822	GPK2	100	5 10⁻⁷	F1
3-A	144	64	SW	-4539	GPK3	50	5 10⁻⁷	F4
3-E	137	72	NE	-4736	GPK3	100	5 10⁻⁷	F2
3-F	0	79	NW	-4754	GPK3	100	5 10⁻⁷	F1
3-G	22	66	NW	-4789	GPK3	100	5 10⁻⁷	F1
3-B /4-E	144	64	NE	-4606	GPK4	50	5 10⁻⁷	F4
4-I	18	75	NW	-4791	GPK4	50	5 10⁻⁷	F1

Figure 9c represents a horizontal slice of the second 3D fracture model. The deterministic fault zones being slightly smaller than the stochastic fractures, they are barely seen. With the greatest density and the largest radius, N2°E-70°W fracture set (F1) is the most represented fracture set in the fracture network.

Preliminary fracture densities have been deduced from the theoretical analysis and then, progressively fitted on the base of the simulation of the various hydraulic tests in the wells and of the circulation tests.

3.5 Appropriate Size of the Flow Model and Boundary Conditions

Preliminary flow runs have been performed in order to determine the optimum size of the 3D model, the appropriate hydraulic boundary conditions in regards with the regional context, and the suitable hydraulic fracture properties.

The size of the 3D model has been chosen in order to integrate the three open holes of the deep reservoir, and to limit the intersections between any potential large deterministic fault zone and the boundary limits of the model. This prevents from having direct hydraulic connections between the external boundary limits and the wells, and forces the fluid to go through the statistical fracture network. The 3D flow model is the following parallelepiped volume:

- 3 km along the North/South axis,

- 2 km along the East/West axis,

- 2.5 km along the Vertical axis, from a -5.8km depth up to a -3.3km depth.

In a horizontal plane, the centre of the model is equidistant to the bottom of GPK2 open hole and to the bottom of GPK4 open hole. The size of this parallelepiped volume is consistent with the size chosen by Baujard and Bruel (2006) for modelling flow in the deep reservoir.

From thermal numerical simulations, Bächler (2003) calculated that the regional flow rate was about 3.10^{-4} m³/s (~1 m³/h), oriented from East towards West. From geochemical fluid analysis, Sanjuan *et al.* (2006) came to the same order of magnitude, with a regional flow rate of about $2.8\ 10^{-4}$ - $3.3\ 10^{-4}$ m³/s, oriented from East towards West. So, the flow rate on the East boundary limit was fixed to this value. The other boundary limits and a first set of fracture hydraulic properties have been chosen so that 1) the head pressures obtained in the reservoir after a flow run in permanent regime remain about hydrostatic, and 2) the fluid conservation equilibrium must be satisfied.

The appropriate boundary limits correspond to a fixed hydrostatic head on each face of the model, except the East face where is fixed a constant 3.10^{-4} m³/s flow rate.

The resulting hydraulic model includes the three wells GPK2, GPK3 and GPK4. The open holes are defined by the depths of their top and bottom. The intersections between the well trajectories and the generated statistical fractures are calculated. Only the deterministic fault zones and the statistical fractures that cut an open hole are hydraulically connected to the corresponding well. Flow rates are imposed in each well.

4. RESULTS

4.2 Flow Model

After a preliminary flow run in permanent regime with the boundary limits detailed above, it is checked that the fluid balance equilibrium is respected. The fluid flow rate enters the model mainly through the top face and exits through the bottom face.

Then, some well tests have been simulated with the reference fracture model. Results are not presented here. The fitting of these well tests yielded to modify step by step the fracture transmissivity and the global storage S_s. In order to take into account the effect of the stimulations performed in the wells, the hydraulic properties of the fractures in the vicinity of the stimulated open holes have also been modified.

4.3 Transport Model

For simulating the five-month circulation test performed in Fall 2005 between the three wells, 10 000 particles equivalent to 150 kg of fluorescein were injected in GPK3. The particles are transported mainly by advection along the flow streamlines. They are tracked and their arrivals in GPK2 and GPK4 or at the boundary limits are monitored with time. To save computing time, recycling is not taken into account in the calculation.

The tracer test results obtained with the first fracture model (Gentier *et al.*, 2009), not presented in details in this paper showed that a far too large amount of tracer arrived into GPK2 so that the concentration of simulated BTC was about 3 times greater than the observed one in GPK2 (Figure 9b).
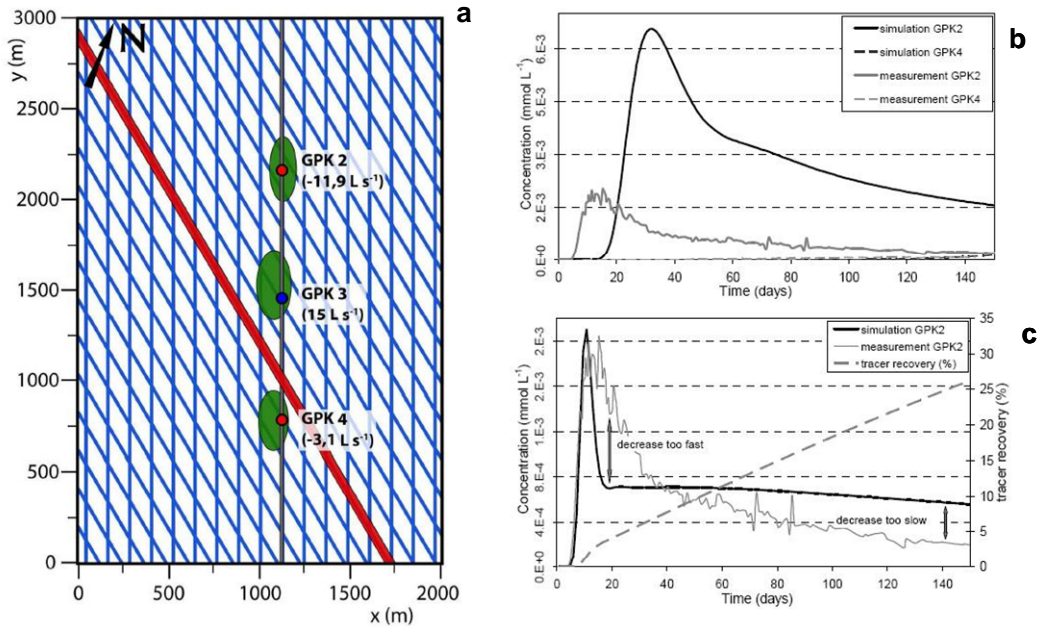
Figure 8 : a) Numerical model (horizontal view) used by Blumenthal *et al.* (2007) and b) reference model and c) adjusted model with best coincidence to the measured data by Blumenthal *et al.* (2007).
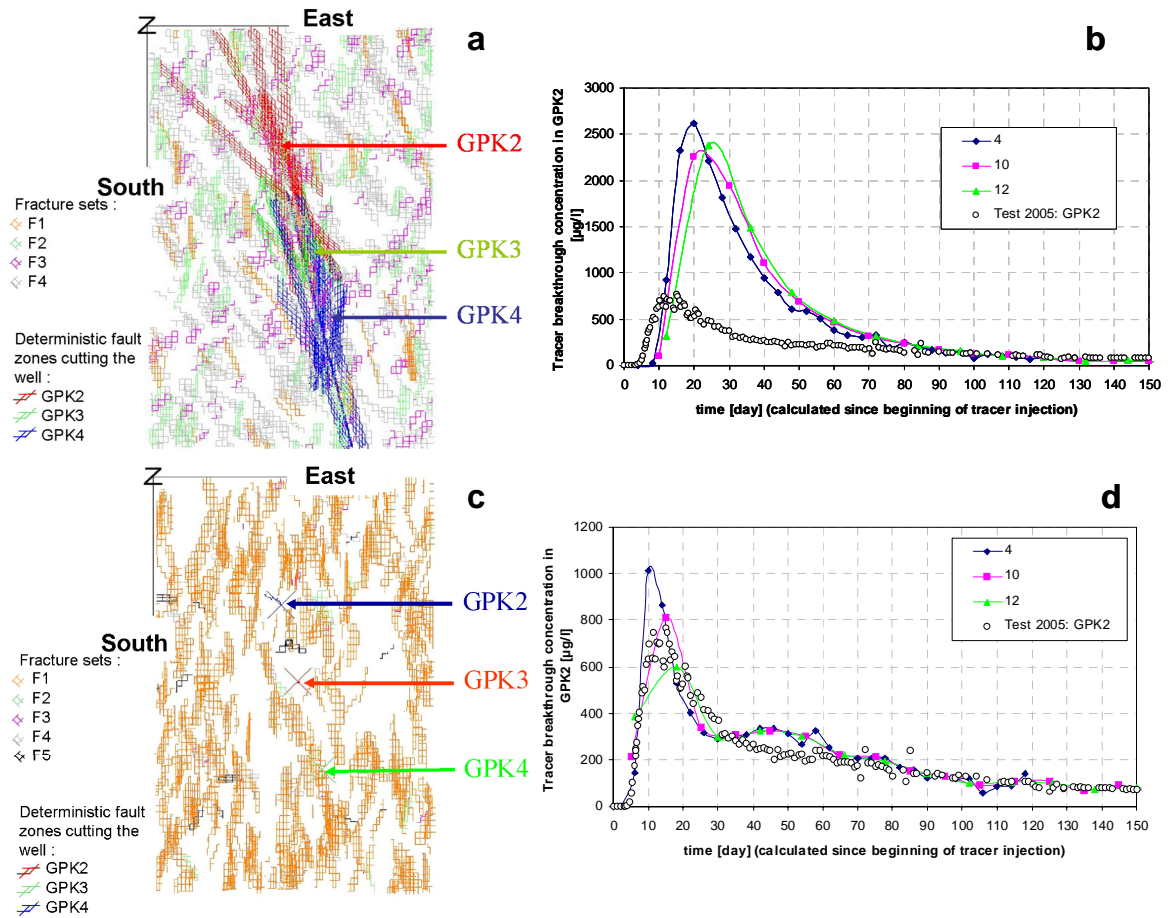

Figure 9: Simulation of five-month circulation test with tracer transport in GPK2 (without any tracer recycling)– Fracture network (a) and Tracer breakthrough curve for the first model (b); Fracture network (c) and Tracer breakthrough curve for the second model (d).

The circle symbols correspond to the *in situ* breakthrough data, whereas the continuous lines correspond to the simulated breakthrough curves. The simulated breakthrough concentration is calculated by counting the number of particles arriving between two dates, at GPK2 or at GPK4, and by dividing the total mass of those particles by the volume of the pumped fluid in the respective wells between these two dates. The three continuous lines, respectively plotted in blue, magenta and green, correspond to three timeframe widths: 4 days, 10 days and 12 days, respectively. This way to calculate the simulated breakthrough concentration curve should be updated by counting a fixed number of particles, rather than by counting the number of particles that arrive between series of fixed dates. This would smooth the shape of the simulated breakthrough curve.

Figure 9d and Figure 10 represent, respectively for GPK2 and GPK4, the two simulated tracer breakthrough concentration curves for the second model.

For GPK2, the fracture model correctly reproduces the first time of arrival (about 5-6 days), as well as the breakthrough peak arrival date (about 15-20 days). To finely fit the time of first arrival and the time of breakthrough peak, a pipe porosity *n* of 10% and a dispersivity of 1 m have been specified to all the pipes constituting the 3D network. The breakthrough peak concentration 800 μg/l, is about the same as the concentration obtained during the *in situ* tracer test. The simulated tracer recovery in GPK2 after the five-month circulation test is about 26% whereas the *in situ* recovery is about 23.5%.

The GPK4 breakthrough is not satisfactorily reproduced. After the five-month circulation test, the simulated GPK4 breakthrough peak (Figure 10) is about twenty-five times greater than the experimental peak and the GPK4 recovery is ~7%, about four times the *in situ* recovery. This indicates that a too large amount of tracer arrives into GPK4, although a correct amount of tracer arrives in GPK2. Moreover, whereas the statistical generation of the fracture network must lead to a homogeneous structure of this fracture network, a slight discrepancy in shape between the two simulated breakthrough curves is observed: the breakthrough peak is broader in GPK4. Attention must be paid to the asymmetric productivity between GPK2 (-12 × 10^{-3} m^3/s) and GPK4 (-3 × 10^{-3} m^3/s) that could explain the difference in the peak magnitude.

If we focus on the GPK2 breakthrough curve, to reach this result, a systematic method has been applied consisting in a detailed analysis of the contribution in the tracer recovery of each statistical fracture set. A series of numerical simulations of the tracer test has been performed. Finally, the role of each fracture set can be illustrated Figure 11 for GPK2. Both fracture sets F1 and F2 have a strong contribution to the GPK2 peak breakthrough as their mean direction, respectively N2°E-70°NW and N162°E-70°NE, potentially create the shortest paths between GPK3 and GPK2. Fracture sets F3 and F4 have a main contribution to the GPK2 breakthrough curve for times greater than 40 and 90 days, respectively, since their mean directions, respectively N42°E-74°NW and N129°E-68°SW, potentially create longer paths than the directions N2°E and N162°E (F1 and F2 sets). A similar analysis can be done for the simulated breakthrough curve of GPK4 (Figure 12). However, the probability of intersection of the N-S striking fracture sets F1 and F2 with GPK4 is important (Figure 5 and Table 2). Because of these important probabilities of intersection, F1 and F2 have a strong contribution to the

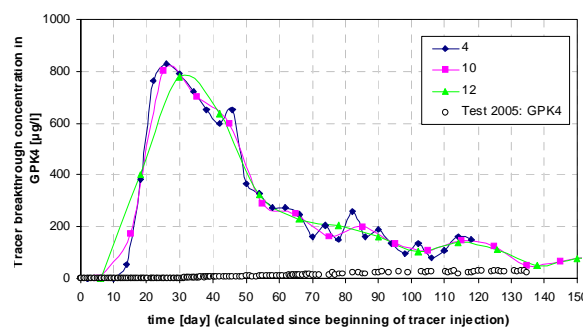GPK4 peak breakthrough of the model (Figure 12), not observed in the experimental curve.

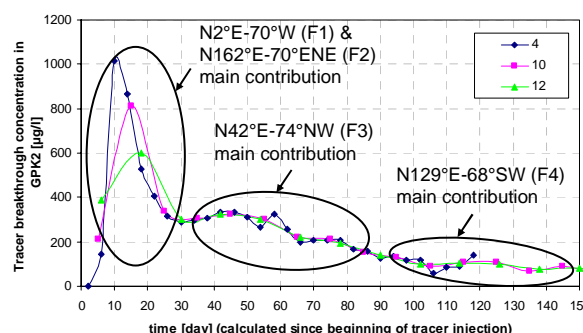**Figure 10: Tracer breakthrough concentration in GPK4 (without any tracer recycling).**

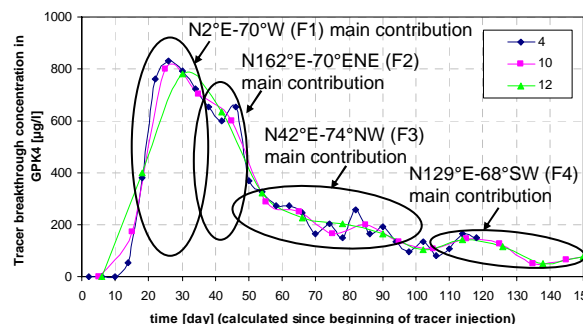**Figure 11: Contribution of each fracture set to the GPK2 tracer breakthrough.**

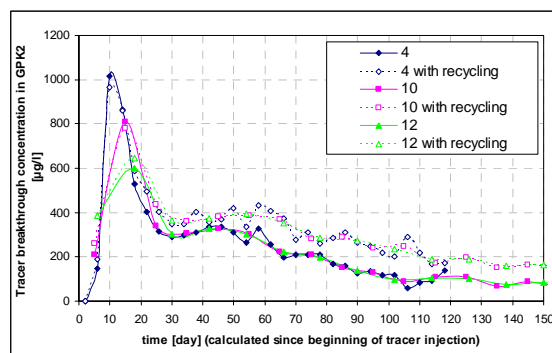**Figure 12: Contribution of each fracture set to the GPK4 tracer breakthrough.**

Figure 13: Tracer breakthrough concentration in GPK2 Impact of the tracer recycling.

Gentier et al.

In the second model (Figure 9c and d), the global intrinsic permeability k [L^2] estimated by the ratio of the transmissivity and the aperture is of the order of $10^{-10} - 10^{-11}$ m^2.

The fracture densities for each set, their radius and their hydraulic properties given Table 4 have been adjusted by fitting the flow and transport tests. Densities chosen in the fracture models are plotted Figure 6 representing the relation between fracture lengths and densities estimated from the probability analysis of intersecting a well (see § 2.2).

The previous breakthrough curves have been simulated without recycling the tracer. The impact of the particle recycling is illustrated Figure 13 for the GPK2 breakthrough curve. With recycling, the breakthrough peak does not change much as, at 15-20 days, very few particles have enough time to circulate twice between GPK2-GPK4 and GPK3. For times greater than thirty days, the GPK2 breakthrough concentration is about one and a half to two times the concentration without recycling so that the recovery is of 35% after 5 months. It can be seen that the simulated GPK2 BTC reproduces not so far from the measured curve *in situ* while the particle recycling is taken into account.

5. DISCUSSION AND CONCLUSIONS

Results obtained from simulation show that the structural model re-analysed and used in the transport model can explain the experimental breakthrough curve of GPK2.

The length of the statistic fractures governs the global connectivity of the network. The connectivity expressed in term of number of intersection by fracture is 7.97 for the first model and 4.92 for the second model. For given fracture lengths the fracture densities for each fracture set introduced in the model are an order of magnitude lower than the densities estimated from the data observed in the well. This could correspond to a realistic ratio between the observed fractures and the fractures hydraulically active. The lengths of the main fault zones identified in the well play also a significant role in the magnitude of the peak by supporting more or less direct connection between the wells GPK3 and GPK4.

The main difference between the first model and the second model lies in the beam of fault zones which strongly increases the recovery via the most direct paths. In this case, our first model is clearly closer to the reference model built by Blumenthal *et al.* (2007) in which the fracture network is constituted by two sets of infinite fractures. However, it differs from the reference model in Blumenthal *et al.* (2007) by the simulation of the concentration recovery after thirty days. As the statistical network constituting the background in our reference model presents a smaller connectivity and permeability, it permits to limit the recovery and to obtain a range close to those observed *in situ*. On the other hand, the limitation of the lengths of the main deterministic fault zones, eliminating the most direct connection between the wells, permits to reduce the magnitude of the peak. It can also be noted that the two models have the same horizontal size and the same order magnitude of the permeability.

In our present model, each of the main fracture sets plays a role very well identified in the evolution of the tracer recovery. The two directions N2°E-70°NW (F1) and N162°E-70°NE (F2) explain the first fast loop of the conceptual model of Sanjuan *et al.* (2006) whereas the two other directions N42°E-74°NW (F3) and N129°E-68°SW (F4) explain the second loop of Sanjuan *et al.* (2006). In

parallel, in the 2D model performed by Blumenthal *et al.* (2007), one of the two fracture sets coincides with the N-S fracture set F1 of our model and the second one (N ~150°E) is intermediate between the fracture sets F2 and F4 of our model.

Finally, results of the model transport seem to lead to fracture network between GPK3 and GP2 without very long main fault zones and with a background requiring at least the four main fractures sets. More in details, two points have to be highlighted. First, in our present model, even if the density of the fifth fracture set is low, the existence of this set is essential to the general connection of the network. Second, the fracture set N°162°E (F2) with a direction close to the F1 N-S direction but an opposite vergence is in fact only hydraulically active if F1 is dense enough. This fracture set appears to contribute to the global connectivity in the vertical direction of the model.

If the proposed fracture model makes the simulation of the GPK2 breakthrough curve possible, it is impossible to reproduce GPK4 breakthrough curve. It is barely impossible to define a unique homogeneous statistical model leading to a simultaneous fit of the two wells. It seems essential to be able to understand what structurally happens between GPK3 and GPK4 before going further in the transport model between the three wells.

Two possibilities can be investigated. First, a real major structure either very conductive or impermeable intersects the flow between GPK3 and GPK4 linked with the microseismic observations made during hydraulic stimulations (zone without microseismic events). Secondly, independently or in parallel, a local evolution of the structural pattern should be envisaged. The work in progress lets assume that a regional evolution of the basic pattern could be a solution. At this stage, it seems that the directions N42°E and N129°E (F3 and F4 sets) could play a more important role between GPK3 and GPK4 than between GPK3 and GPK2. This could be related to variations in terms of density as supposed by the differences in the reconstructed densities from GPK3 and GPK4 (Table 3), or in terms of hydraulic properties of the various fracture sets. The initial regional fracture densities or hydraulic properties can change progressively laterally, or a compartmentalisation of the volume can be considered as illustrated at Figure 14. Another point which must also be considered to understand the recovery curve for GPK4 is the effect of the leaks in the GPK4 casing.
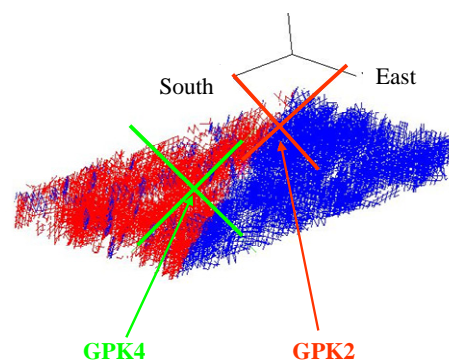

Figure 14: Compartmentalisation of the fracture density and hydraulic properties – View of the pipe conductivities.

In parallel to the evolution of the structural pattern, another point should be investigated: the impact of the hydraulic

and/or chemical stimulation on the permeability in the vicinity of the wells. The attempts based on the global increase of the permeability in a given radius around the wells, carried out during the successive fittings of the hydraulic properties to integrate the history of each well were unfruitful. Similarly, Blumenthal *et al.* (2007), to obtain the best fit for their curve, keep the permeability of the stimulated zones at the same level than those of the fracture sets, modifying only the porosity of the stimulated zones. Other works led in parallel (Rachez *et al.*, 2009) could improve this point by integrating a more focus impact of the hydraulic stimulation in relation with the hydromechanical behaviour of the stimulated fault zones.

In conclusion, the fracture database of the Soultz-sous-Forêts has been re-investigated in order to define a proper fracture model able to satisfactorily reproduce the *in situ* tracer test that accompanied the 2005 circulation test between GPK3 and GPK2-GPK4. The resulting conceptual fracture model is made of five main statistical fracture sets, whose directions are consistent with the structural context, as well as some deterministic fractures that connect the statistical fracture sets to the boreholes. It constitutes a first basic model based on a realistic structural model and presenting all the potentialities to evolve to a global model integrating the four wells in the Soultz-sous-Forêts site (including GPK1 and the upper part of the reservoir). With such a model, it would be possible to study *scenarios* implicating the four wells GPK1, GPK2, GPK3 and GPK4.

ACKNOWLEDGEMENTS

REFERENCES

Aquilina, L., Rose, P., Vaute, L., Brach, M., Gentier, S., Jeannot, R., Jacquot, E., Audigane, P., Tran-Vie, T., Jung, R., Baumgktner, J., Baria, R. and Gérard A. (1998) - A tracer test at the Soultz-sous-Forêts Hot Dry Rock Geothermal Site. Proceedings, Twenty-Third Workshop on Geothermal Reservoir Engineering, Stanford University, Stanford, California, January 26-28, 1998, SGP-TR-15, p. 343-350.

Bächler, D. (2003) – Coupled Thermal-Hydraulic-Chemical modelling at the Soultz-sous-Forêts HDR reservoir (France), Ph.D. thesis, Swiss Federal Institute of Technology Zürich, 151 pp.

Baujard C. and Bruel D. (2006) – Numerical study of the impact of fluid density on the pressure distribution and stimulated volume in the Soultz HDR reservoir. Geothermics, 35, p. 607-621.

Bergerat, F. (1985) - Déformations cassantes et champs de contraintes tertiaires dans la plateforme européenne., Ph.D. thesis, Université Pierre & Marie Curie, Paris VI.

Blumental, M., Kuhn, M., Pape, H., Rath, V. and Clauser C. (2007), Hydraulic model of the deep reservoir quantifying the multi-well tracer test. Proceedings of the EHDRA scientific conference 28-29 June 2007, Soultz-sous-Forêts, France.

Cuenot, N. , Dorbath, C. and Dorbath, L. (2008) – Analysis of Microseismicity Induced by Fluid Injections at the EGS Site of Soultz-sous-Forêts (Alsace, France): Implications for the Characterization of the Geothermal

Reservoir properties, Pure appl. Geophys. 165, p. 797-828.

Dezayes, C., Chevremont, P., Tourlière, B., Homeier, G. and Genter, A. (2005) - Geological study of the GPK4 HFR borehole and correlation with the GPK3 borehole (Soultz-sous-Forêts, France) - Final Report, Report BRGM Orléans, France, RP-53697-FR, 97 p.

Dezayes, C. and Genter A. (2008), Large-scale fracture zone network based on Soultz borehole data. Proceedings of the EHDRA scientific conference 24-25 September 2008, Soultz-sous-Forêts, France.

Edel, J. B., Schulmann, K. and Rotstein, Y. (2007) - The Variscan tectonic inheritance of the Upper Rhine Graben: evidence of reactivations in the Lias, Late Eocene-Oligocene up to the recent, International Journal of Earth Sciences, p.305-325.

Gentier, S., Sanjuan, B., Rachez, X., Tran Ngoc, T. D., Beny, C., Peter-Borie, M. and Souque, C. (2009) - A progress in the comprehension of fluid circulation in the site of Soultz-sous-Forêts : BRGM contribution to the STREP "EGS Pilot Plant" - Final Report, Report BRGM Orléans, France, BRGM/RP-57437-FR, 97 p. + annexes.

Gessner, K., Kühn, M., Rath, V., Kosack, C., Blumenthal, M., and Clauser, C. (2009)- Coupled process models as a tool for analysing hydrothermal systems. Surv Geophys., 30, 133-162.

Illiès, J.H. (1972) – The Rhine Graben rift system – Plate tectonics and transform faulting, Geophysical Surveys, 1, p. 27-60.

Itasca (2006) – 3FLO Version 2.31, User's manual. Itasca Consultants SAS, Ecully, France.

Louis C. (1976), Introduction à l'hydraulique des roches. Thèse de doctorat d'état es-sciences physiques de l'université Pierre et Marie Curie, 115 p & annexes.

Rachez, X. and Gentier, S. (2009) – 3D hydromechanical behaviour of a stimulated rock mass. In Proceedings World Geothermal Congress 2010, Bali, Indonesia, 25-29 April 2010.

Sanjuan, B., Pinault, J.-L., Rose, P., Gérard, A., Brach, M., Braibant, G., Crouzet, C., Foucher, J.-C., Gautier, A. and Touzelet, S. (2006) - Tracer testing of the geothermal heat exchanger at Soultz-sous-Forêts (France) between 2000 and 2005. Geothermics, 35, n°5-6, 622-653.

Sausse, J., Desayes, C. and Genter, A. (2007) - From geological interpretation and 3D modelling to the characterization of the deep seated EGS reservoir of Soultz (France). Proceedings European Geothermal Congress 2007, Unterhaching, Germany, May 30-June 1, 2007.

Sausse, J., Dezayes, Ch., Dorbath, L., Genter, A. and Place, J.(2008). 3D fracture zone network at Soultz based on geological data, Image logs, microseismic events and VSP results, Proceedings of the EHDRA scientific conference 24-25 September 2008, Soultz-sous-Forêts, France.

Schulmann, K. Jezek, J. and Venera, Z. (1997) Perpendicular linear fabrics in granite: markers of combined simple shear and pure shear flows? In: Bouchez JL, et al (eds) Granites from segregation of

melt to emplacement fabrics. Kluwer Academic Publisher, Dordrecht, pp 159–176.

Schumacher M. E. (2002) - Upper Rhine Graben: role of pre-existing structures during rift evolution. Tectonics 21(1).

Valley, B. C. (2007) – The relation between natural fracturing and stress heterogeneities in deep-seated crystalline rocks at Soultz-sous-Forêts (France). EHT PhD thesis, 260 pp.

Villemin, T. (1986) - Tectonique en extension, fracturation et subsidence : Le Fossé Rhénan et le bassin de Sarre-Nahe., Ph.D. thesis, Paris VI, 270 pp.

Ziegler, P. A. (1990) - Geological Atlas of Western and Central Europe, 239 pp., Shell Int. Pet. Maatschappij, Geol. Soc. Publ. House, Bath, UK.